

Invited Review

## Using Sulfur as metallicity tracer in galaxies

A. I. Díaz<sup>1,2</sup>

<sup>1</sup> *Department of Theoretical Physics, Universidad Autónoma de Madrid, Spain* and <sup>2</sup> *CIAFF, Universidad Autónoma de Madrid, Spain*

**Abstract.** We review the present methodology for the use of Sulfur as global metallicity tracer in galaxies, which allows performing a complete abundance analysis using mainly the red to near infrared spectral region, and extending the range of directly derived abundances up to 5 times the S solar photospheric value. The empirical calibration of Sulfur via the S<sub>23</sub> parameter is also reviewed.

**Key words:** galaxies: abundances — galaxies: ISM — techniques: imaging spectroscopy

### 1. Introduction

Oxygen is the most abundant element after Hydrogen and Helium. It is produced in high mass stars and hence it is returned to the ISM in a short time scale. Therefore, when measured in gaseous nebulae, its abundance can be associated with “present day abundances”. In the case of nebulae ionized by young, hot stars, given the range of their effective temperatures, Oxygen is present in the form of O<sup>+</sup> and O<sup>++</sup>. When these ions collide with free electrons they get excited to higher energy levels and subsequently decay through radiative transitions producing forbidden emission lines of [OII] ( $\lambda\lambda 3727, 29 \text{ \AA}$ ) and [OIII] ( $\lambda\lambda 4959, 5507 \text{ \AA}$ ), readily accessible in the optical spectral region. Therefore the metallicity of gaseous nebulae has traditionally been traced by Oxygen. However, their use is restricted to abundances lower than solar since these lines act as very effective coolants and, at high abundances, nebulae become too cool for the lines to be detected. So, what about using Sulfur? Sulfur is also produced in massive stars and its yield is supposed to follow that of Oxygen. Although less abundant than Oxygen, in principle, sulfur can also be used as abundance tracer providing similar information and, since the [SII] ( $\lambda\lambda 6716, 6731 \text{ \AA}$ ) and [SIII] ( $\lambda\lambda 9069, 9532 \text{ \AA}$ ) lines take place at the red spectral region, they present several interesting observational advantages: they are less contaminated by stellar absorption lines from metals (there are many more metal lines in the blue) and less affected by reddening. The lines can be measured relative to nearby Hydrogen recombination lines, thus minimizing the effects of reddening and flux calibration. Furthermore, there is almost no depletion of Sulfur onto dust grains in the diffuse ISM. But, most importantly: the [SIII] lines are clearly detected at high abundances where the “strong” [OIII] lines are very weak or almost undetectable due to the low electron temperature.

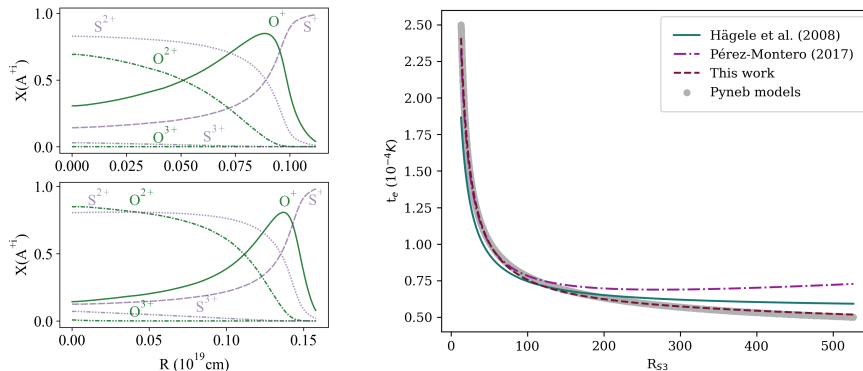


Figure 1. *Left:* Ionization structure of a Cloudy model of low density ( $100 \text{ cm}^{-3}$ ) HII regions of half solar abundance ionized by a 5 Ma star cluster, representative of the objects in the DHR sample (lower panel) and HII regions of low metallicity ( $Z=0.004$ ) ionized by a young (1 Ma) star cluster of  $10^5 M_{\odot}$ , representative of the objects in sample HII Gal (lower panel). *Right:* The Sulfur temperature,  $T_e([\text{SIII}])$  as a function of the line ratio  $R_{S3}$ , defined in the text.

The two samples selected for study consist of nebulae ionized by young massive stars located in the disks of spiral galaxies and dwarf galaxies dominated by star formation bursts, henceforth called DHR and HII Gal respectively. High quality spectroscopic data have been taken from the literature and cover at least, the spectral range from  $\lambda 3700 \text{ \AA}$  to  $\lambda 9600 \text{ \AA}$  at moderate to high resolution. In all cases the  $[\text{SIII}]$  line at  $\lambda 6312 \text{ \AA}$  has been measured and, in combination with the strong nebular lines at  $\lambda \lambda 9069, 9532 \text{ \AA}$ , allows the derivation of the electron temperature  $T_e([\text{SIII}])$ .

## 2. Direct abundance derivation: Oxygen vs Sulfur

The intensities of forbidden lines, as the ones we are talking about, depend exponentially of the electron temperature,  $T_e$ . Different ions originate in regions with different  $T_e$  and a certain ionization structure for the nebula has to be assumed. In the case of Oxygen,  $T_e([\text{OIII}])$  is derived from the ratio of auroral to nebular lines at  $\lambda 4363 \text{ \AA}$  and  $\lambda \lambda 4959, 5007 \text{ \AA}$ . Most of the O is in the form of  $\text{O}^+$  and  $\text{O}^{2+}$  and their relative contributions to the total O/H abundance depends on the degree of ionization of the nebula. Only for exceptionally high excitation objects, those showing HeII emission at  $\lambda 4686 \text{ \AA}$ , a small contribution by  $\text{O}^{3+}$  might be present. In the case of Sulfur,  $T_e([\text{SIII}])$  is derived from the ratio of auroral to nebular lines at  $\lambda 6312$  and  $\lambda \lambda 9069, 9532 \text{ \AA}$ . Most of the S is also in the form of  $\text{S}^+$  and  $\text{S}^{2+}$ , but in most cases  $\text{S}^{2+}$  is the dominant specie. However, a certain contribution by  $\text{S}^{3+}$  is expected in high excitation objects for which ionization correction factors (ICF) have to be derived.

Regarding the ionization structure, a three-zone approximation is usually assumed for the derivation of the Oxygen abundance, where  $\text{O}^{2+}$  and  $\text{O}^+$ ,  $\text{S}^+$  are

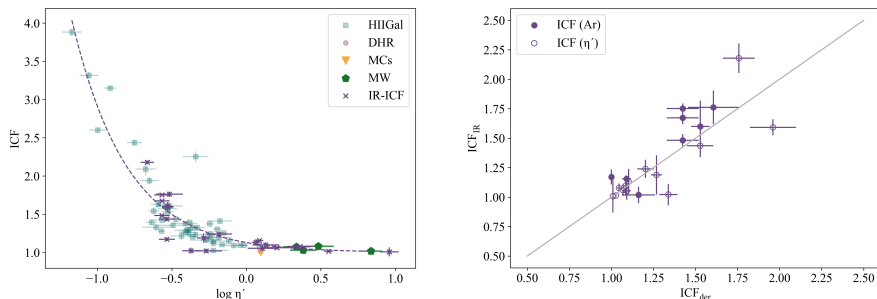


Figure 2. *Left:* Relation between the derived ICF and the  $\eta'$  parameter. As can be seen, the ICF has a value  $\simeq 1$  for  $\eta' > 1.0$ . *Right:* Comparison of the IR derived values of the Sulfur ICF with the ones calculated in this work. For objects labelled as ICF(Ar) they have been calculated from the derived  $Ar^{2+}/Ar^{3+}$  ratio and for objects labelled ICF( $\eta'$ ) from IR data.

produced in high and low ionization regions respectively, characterized by temperatures  $T_e([OIII])$  and  $T_e([OII])$ ;  $S^{2+}$  is assumed to be produced in an intermediate excitation zone characterized by  $T_e([SIII])$ . In the case of Sulfur, Figure 1 (left panel) shows the ionization structure computed from photo-ionization models for two cases representative of the objects in each of the studied samples. In the two cases, both  $S^+$  and  $S^{2+}$  ions can be seen to overlap in a transition zone that encompasses almost the whole nebula. According to this, we have assumed only two zones:  $S^+$ ,  $S^{2+}$ ,  $O^+$  are formed in the same region, characterized by  $T_e([SIII])$  while  $S^{3+}$ ,  $O^{2+}$  are formed in a higher ionization zone characterized by  $T_e([OIII])$ .

Following this description we have derived the  $S^+/H^+$  and  $S^{2+}/H^+$  ionic abundances of 256 independent observations of disc HII regions (including regions in The Milky Way Galaxy, labelled MW, and the Magellanic Clouds, labelled MC) and 95 independent observations of HII galaxies, mostly compact, some of them with several star-forming knots. We have also derived Oxygen abundances for those regions with data on the  $[OIII] \lambda 4363 \text{ \AA}$  line, allowing to derive  $T_e([OIII])$ . The software package PyNeb (Luridiana et al., 2015) has been used with the atomic coefficients listed in Fernández et al. (2018).

The  $S^{2+}$  electron temperature,  $T_e([SIII])$  has been derived from the ratio of the nebular to auroral  $[SIII]$  line intensities ( $R_{S3} = I(\lambda 9069 + \lambda 9532)/I(\lambda 6312)$ ). We have used PyNeb to calculate  $T_e([SIII])$  extending the temperature range down to 5500 K, since most expressions quoted in the literature do not apply to electron temperatures lower than about 8000 K, too high for many disk HII regions present in our sample (see Figure 2, right panel).

Total S/H abundances are found as:

$$S/H = ICF \times \frac{S^+ + S^{2+}}{H^+} \quad (1)$$

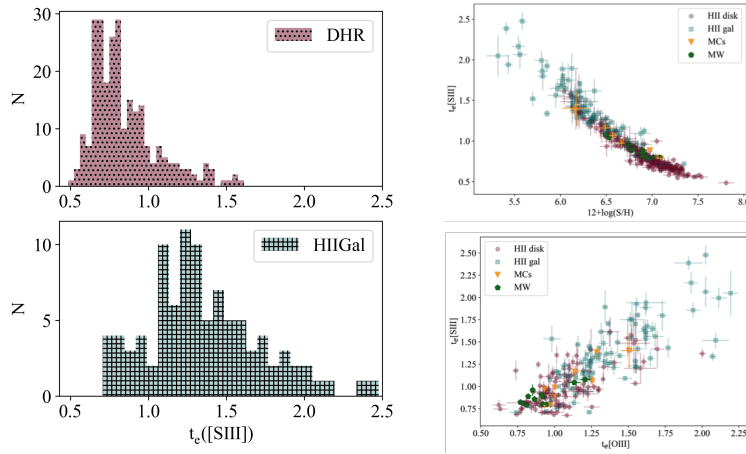


Figure 3. *Left:* Distribution of the derived Sulfur temperature,  $T_e([\text{SIII}])$ , for the two samples studied, as labelled. *Right:* Correlation between the electron temperature, as measured by  $T_e([\text{SIII}])$ , and the total Sulfur abundance:  $12 + \log(\text{S}/\text{H})$  (upper panel) . Empirical relation between  $[\text{SIII}]$  and  $[\text{OIII}]$  electron temperatures (lower panel).

where ICF is the ionization correction factor for Sulfur. Several schemes have been proposed for its derivation (see for example Dors et al., 2016), most of them based on the ionization potential of Oxygen ions as compared to those of Sulfur. Our own proposal involves the relation found from photo-ionization models between the ionic ratios of Ar and S in contiguous ionization stages:  $\text{Ar}^{2+}/\text{Ar}^{3+}$  vs.  $\text{S}^{2+}/\text{S}^{3+}$  (Fernández et al., 2018) . The application of the procedure requires the measurement of the  $[\text{ArIII}]$  and  $[\text{ArIV}]$  emission lines at  $\lambda 7135$  and  $\lambda 4740$  Å respectively.

The ICF shows a certain dependence on the hardness of the ionizing radiation field which can be explored using the  $\eta'$  parameter defined by Vilchez & Pagel (1988) as:

$$\eta' = \frac{[\text{OII}]/[\text{OIII}]}{[\text{SII}]/[\text{SIII}]}$$

The relation between the derived ICF and  $\eta'$  is shown in Figure 2 (left panel). For objects without data on the  $[\text{ArIV}]$   $\lambda 4740$  Å line we have used this relation to estimate the ICF. For some objects of the sample, there are data on the IR  $[\text{SIV}]$  line at  $10.8 \mu\text{m}$ . For those objects we have derived the ICF directly and they compare well with our estimates 2 (right panel).

### 3. Results and discussion

#### 3.1. Sample characteristics

Figure 3 (left panel) shows the  $T_e([\text{SIII}])$  distribution for the two studied samples.

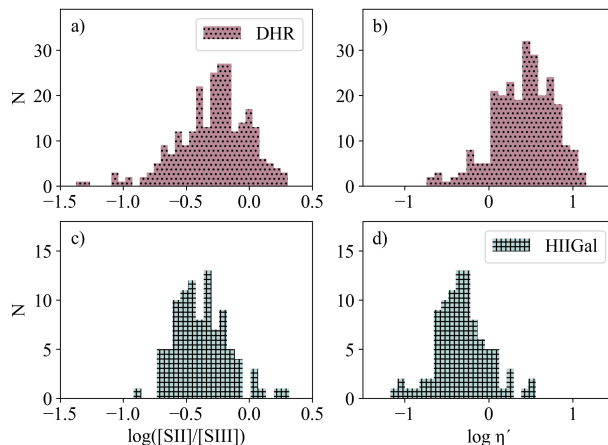


Figure 4. Distribution of the  $[\text{SII}]/[\text{SIII}]$  excitation ratio, taken as a proxy for ionization parameter (left panels), and the  $\eta'$  parameter, taken as a proxy for the ionizing temperature (right panels), for DHR objects (upper panels) and HII Gal objects (lower panels).

The electron temperature of the ionized gas has different distributions for the two studied samples with median  $T_e([\text{SIII}])$  values of 7900 K for DHR and 13000 K for HII Gal objects which reflects the different average metallicities of the objects in the two samples. The effect of Sulfur ions as cooling agents is evident by the good correlation shown between the total Sulfur abundance and the electron temperature as measured by  $T_e([\text{SIII}])$  (Figure 3 (upper right panel) which is the base of the empirical calibration presented below). A certain number of regions also provide measurements of the  $[\text{OIII}]$  line at  $\lambda 4363 \text{ \AA}$  so that  $T_e([\text{OIII}])$  can also be derived. The relation between the two temperatures,  $T_e([\text{SIII}])$  and  $T_e([\text{OIII}])$  is shown in Figure 3 (lower right panel).

The two samples show rather similar distributions regarding excitation with median values of  $\log([\text{SII}]/[\text{SIII}])$  of -0.25 and -0.38 for DHR and HII Gal which, using the calibration by Diaz et al. (1991) correspond to ionization parameter values,  $\log u$ , of -2.56 and -2.34 respectively. However, they show very different distributions regarding the hardening of the ionizing radiation with median values of  $\log \eta'$  of 0.45 for DHR and -0.36 for HII Gal, implying equivalent effective temperatures of 38000 K and 55000 K respectively. The different distributions of ionizing temperatures seems to correspond to a real effect probably related to the nature of the ionizing clusters with HII Gal being characterized by their low metallicities and young ages, and DHR regions showing higher abundances (up to the solar values and maybe beyond) and, in average, being more evolved. Both high stellar metallicities and older ages would lead to lower ionizing star temperatures (see Figure 4).

### 3.2. Directly derived abundances

Figure 5 shows the contribution of the  $\text{S}^+$  and  $\text{S}^{2+}$  ions to the total Sulfur abundance. For both samples,  $\text{S}^{2+}$  is found to be the dominant ionization specie

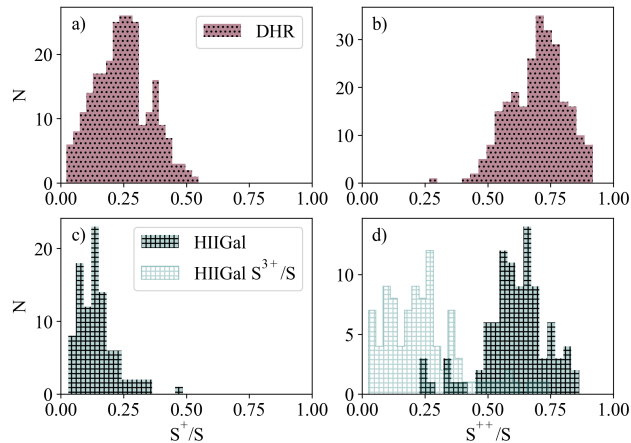


Figure 5.  $S^+$  (left panels) and  $S^{++}$  (right panels) contributions to the total S/H abundance for the two samples as labelled. The contribution of  $S^{3+}$  in the HII Gal sample is shown in the lower right panel in light green.

as can be seen in the right panel of the figure, with  $S^{2+}/S$  median values of about 0.7. This fact justifies the assumption of  $T_e([SIII])$  as the representative electron temperature for the ionized regions.

For DHR objects only two species,  $S^+$  and  $S^{++}$  coexist, and the distributions are mirrored images. In the case of HII Gal objects, this is not the case since there is a certain contribution by  $S^{3+}$  that can be seen in the lower right panel of the figure in light green color.

The S/H distributions in both samples are rather different with median values that differ by  $\approx 0.7$  dex. The highest abundance found is  $12+\log(S/H)=7.82\pm 0.08$ , i.e., about 5 times the solar photospheric value ( $12+\log(S/H)_\odot = 7.12$ ; Asplund et al., 2009). The lowest Sulfur abundances, about 2% of the solar one, are found amongst objects in the HII sample..

The relation between the functional parameters and the S/H abundance is shown in Figure 6. Contrary to what is commonly assumed, no relation is found between ionization parameter and metallicity as traced by Sulfur (see the left panel of the figure). However, there is a clear correlation between  $\eta'$  and metallicity (see the right panel of the figure), showing that HII galaxies are ionized by hotter sources than disk HII regions, which, as mentioned above, can be understood in terms of global metallicity (ionizing stars of higher metallicity are cooler) and age (**disc HII regions** are probably more evolved, and their ionizing stars have lower masses and temperatures).

For the objects with the necessary data, it is possible to derive both the Oxygen and Sulfur abundances which allows to test the assumption of the constancy of the O/S ratio at about the solar ratio,  $\log(S/O)_\odot \approx -1.56$ , if the Sulfur yield would follow that of oxygen. The derived S/O ratio can be seen in Figure 7 that shows: **(1)** a trend of increasing S/O with increasing S/H abundance for the HII Gal sample, which could be due to the increase of oxygen depletion with

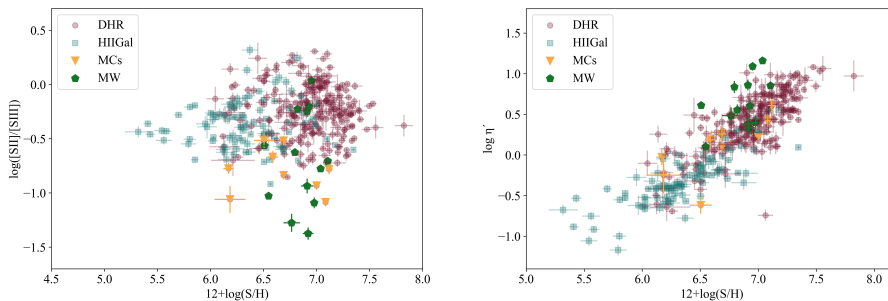


Figure 6. *Left*: Relation between  $\log([SII]/[SIII])$ , taken as a proxy for  $\log u$ , and Sulfur total abundance. *Right*: Relation between  $\log(\eta')$ , taken as a proxy for ionizing temperature, and Sulfur total abundance.

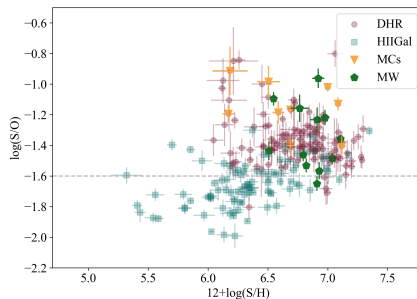


Figure 7. S/O relation against the total abundances of Sulfur.

increasing metallicity. On the other hand, the disk HII regions seem to start at a high value of S/O and follow a decreasing trend with increasing metallicity.

### 3.3. Empirical calibrations

The auroral lines are intrinsically weak and difficult to detect. At high metallicity,  $T_e$  is too low to produce any significant auroral line. However, it is possible to use the cooling properties of the ionized gas in order to produce empirical calibrations that relate emission-line intensity ratios of strong lines to the abundance of a given element. This has been done traditionally for Oxygen. One of the most popular calibrators is  $R_{23}$  defined as the sum of the intensities of the  $[OII]\lambda\lambda 3727, 29 \text{ \AA}$  and  $[OIII]\lambda\lambda 4959, 5007 \text{ \AA}$  normalized to that of  $H\beta$  (Pagel et al., 1979), that has been calibrated against directly derived abundances, which is possible only for low metallicity regions, and results from photo-ionization models in the high metallicity range. The relation obtained is two-folded, since when the O abundance increases substantially, the  $T_e$  in the nebula decreases and the emission lines become weaker. This does not happen for lower abundances where the cooling is dominated by free-free emission from Hydrogen and the relation has a positive slope.

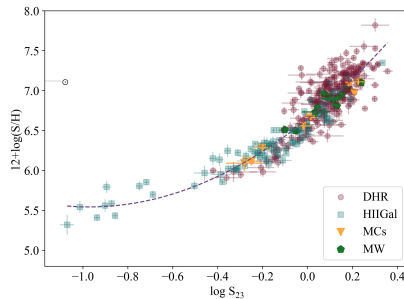


Figure 8. The calibration of the  $S_{23}$  parameter against the total S/H abundance.

But these empirical abundance calibrations can also be done using other strong emission lines (or a combination of several), and/or different abundance tracers. Since the strong nebular lines of Sulfur [SII]  $\lambda\lambda 616, 31 \text{ \AA}$  and [SIII]  $\lambda\lambda 9069, 9532 \text{ \AA}$  are analogous to those of Oxygen a similar calibration can be done using the  $S_{23}$  parameter defined by  $S_{23} = ([SII]6717, 31 + [SIII]9069, 9532)/H_{\beta}$  (Vilchez et al., 1988) as abundance indicator. This parameter, presents several advantages with respect to  $R_{23}$ : (1) the calibration remains single-valued up to, at least, solar abundances; (2) the lines are observable even at over-solar abundances; and (3) the effects of reddening are minimal.

The calibration of the  $S_{23}$  parameter in terms of the total S/H abundance is shown in Figure 8. A second order polynomial fit yields the relation:

$$12 + \log\left(\frac{S}{H}\right) = (6.636 \pm 0.011) + (2.202 \pm 0.050) \cdot \log S_{23} + (1.060 \pm 0.098) \cdot (\log S_{23})^2 \quad (2)$$

with a typical deviation of 0.18.

The  $S_{23}$  parameter is found to be independent of the ionization parameter, but shows a certain dependence of  $\eta'$  (see Figure 9) and, as it is evident from Figure 8, the dispersion in the  $S_{23}$  calibration is larger than accounted for by observational errors.

To find the responsible for the intrinsic dispersion we have performed a principal component analysis. The obtained result indicates clearly the independence of the ionization parameter,  $u$ , from the rest of the variables and hence it has been excluded from further analysis. The relation among the other three parameters involved explains 76 % of the variance shown by the data set, with very similar weights by each of them (see Figure 10). This tendency is maintained in the analysis of the calibration residuals. According to this, it is possible to make a correction to the S/H abundance derived from the  $S_{23}$  calibration to take into account the correlation of its residuals with  $\eta'$ .



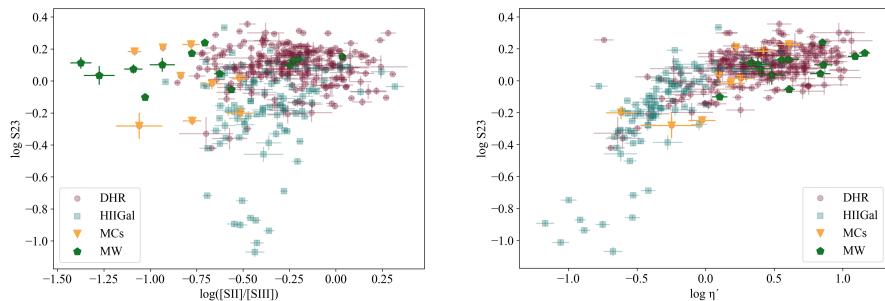


Figure 9. *Left:* Relation between  $\log([SII]/[SIII])$ , taken as a proxy for  $\log u$ , and the  $S_{23}$  parameter. *Right:* Relation between  $\log(\eta')$ , taken as a proxy for ionizing temperature, and the  $S_{23}$  parameter.

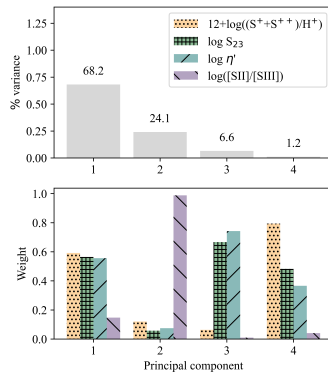


Figure 10. Results of the PCA showing the percentage contribution of each principal component to the total variance shown by the data set (upper panel) and the normalized relative weights of each parameter, as labelled, to each principal component (lower panel).

#### 4. Conclusions

In this work we have reviewed the methodology for the use of Sulfur to trace chemical abundances in ionized nebulae by means of spectroscopy in the red-to-near infrared wavelength range, from 600 to 980 nm. Two samples of high quality, moderate-to-high spectral resolution published data have been selected for study: (1) nebulae ionized by young massive stars located in the disks of spiral galaxies and (2) dwarf galaxies dominated by star formation bursts. The two samples show overlapping ranges of ionization parameter, however they differ widely in the value of the parameter  $\eta'$  indicating that HII Gal objects contain hotter ionizing stellar populations.

For all the objects, we have derived the abundances of Sulfur by direct methods assuming an ionization structure composed of two zones: a low/intermediate excitation zone where  $S^{++}$  and  $S^+$  originate and a high ionization zone where  $S^{3+}$

might be formed. For both samples,  $S^{2+}$  is found to be the dominant ionization specie. In order to correct for unseen ionization stages in high excitation objects, we have used an ICF scheme based on the  $Ar^{3+}/Ar^{3+}$  ratio which requires the detection and measurement of the  $[ArIV]\lambda 4740 \text{ \AA}$ , finding a good correlation between the Sulfur ICF and the parameter  $\eta'$ . We have applied this correlation to estimate the ICF for those objects without data on the  $[ArIV]$  line. Most DHR objects show ICFs close to unity and therefore no ICF correction needs to be applied.

The S/H abundance distributions in both samples span different ranges with median values of  $12+\log(S/H)$  of 6.27 for the HII Gal sample, and 6.92 for the DHR sample with abundances reaching up to 5 times the solar photospheric value. At this high abundances, the  $[OIII] \lambda 4363 \text{ \AA}$  auroral line is not detected and hence these objects would had been missed from the distribution had Oxygen been chosen as abundance tracer. The lowest Sulfur abundances, about 2% of the solar value, have been found amongst HII Gal objects. A good correlation exists between the Sulfur abundance and  $\eta'$  with low metallicity objects being ionized by stellar clusters of higher effective temperature (lower  $\eta'$  values).

For objects with all the necessary data, directly derived Oxygen abundances have been calculated, so that the behavior of the S/O ratio could be explored. Most HII Gal objects show S/O ratios below the solar value and a trend is found for an increased S/O ratio with increasing Sulfur abundance. On the other hand, DHR sample objects show S/O ratios larger than solar and show a tendency for lower S/O ratios at higher metallicities. More detailed work is needed, mostly in the high-metallicity regime, in order to assess the reality of these trends and understand their causes.

**Acknowledgments.** I would like to warmly acknowledge the help of Sandra Zamora in the preparation of this review. This research has been supported by Spanish grants AYA2016-79724-C4-1-P and PID2019-107408GB-C42.

## References

- Asplund M., Grevesse N., Sauval A. J., Scott P., 2009, *ARA&A*, **47(1)**, 481  
 Diaz A. I., Terlevich E., Vilchez J. M., Pagel B. E. J., Edmunds M. G., 1991, *MNRAS*, **253**, 245  
 Dors O. L., Pérez-Montero E., Hägele G. F., Cardaci M. V., Krabbe A. C., 2016, *MNRAS*, **456(4)**, 4407  
 Fernández V., Terlevich E., Díaz A. I., Terlevich R., Rosales-Ortega F. F., 2018, *MNRAS*, **478(4)**, 5301  
 Luridiana V., Morisset C., Shaw R. A., 2015, *A&A*, **573**, A42  
 Pagel B. E. J., Edmunds M. G., Blackwell D. E., Chun M. S., Smith G., 1979, *MNRAS*, **189**, 95  
 Vilchez J. M., Pagel B. E. J., 1988, *MNRAS*, **231**, 257  
 Vilchez J. M., Pagel B. E. J., Diaz A. I., Terlevich E., Edmunds M. G., 1988, *MNRAS*, **235**, 633